Journal of the European Ceramic Society 22 (2002) 1587–1600

www.elsevier.com/locate/jeurceramsoc

Boron nitride–silicon carbide interphase boundaries in silicon nitride–silicon carbide particulate composites

Kevin M. Knowles[a,*], Servet Turan[b]

[a]*University of Cambridge, Department of Materials Science and Metallurgy, Pembroke Street, Cambridge CB2 3QZ, UK*
[b]*Anadolu University, Department of Ceramics Engineering, Iki Eylül Kampüsü, 26470 Eskişehir, Turkey*

Received 1 August 2001; accepted 13 October 2001

Abstract

Interphase boundaries between SiC and *h*-BN grains in hot isostatically pressed Si_3N_4–SiC particulate composites made from both as-received powders and deoxidised powders, in which sub-micron size *h*-BN particles occur as a contaminant, have been characterised using transmission electron microscopy techniques. Most of the *h*-BN grains observed were aligned with respect to SiC grains so that (111) 3C SiC and (0001) α-SiC planes were parallel to (0001) *h*-BN planes. The *h*-BN–SiC interphase boundaries in the composites made from as-received powders were covered with thin silica-rich intergranular films, in contrast to the interphase boundaries in the composites made from deoxidised powders. These observations are discussed in the light of models for the formation of intergranular amorphous films in ceramic materials, geometric considerations for low interfacial energies and the possible bonding at *h*-BN–SiC interphase boundaries free of intergranular films.

Keywords: BN; Electron microscopy; Interfaces; Microstructure-final; SiC; Si_3N_4

1. Introduction

There are a number of reasons for incorporating hexagonal boron nitride (*h*-BN: $a = 2.5044$ Å, $c = 6.6562$ Å) into ceramic matrices. One is to increase the thermal shock resistance of a ceramic matrix.[1–6] A second reason is to improve the fracture toughness of the ceramic matrix.[7–10] *h*-BN has also been examined as a replacement for graphite as a 'weak' interfacial coating for fibres in Si–C–O fibre-reinforced glass ceramics.[11]

While such reasons provide a rationale for wanting to understand the behaviour of interphase boundaries formed between *h*-BN and ceramic matrices such as silicon carbide (SiC) and silicon nitride (Si_3N_4), there are remarkably few reports in the literature on either the structure of such interfaces or their mechanical and thermal behaviour. In recent work on the characterisation of particulate Si_3N_4–SiC composites, small *h*-BN grains were found inside SiC grains and Si_3N_4 grains, and at both grain boundaries and interphase boundaries.[12] These provide an ideal opportunity to examine boundaries between *h*-BN and both SiC and Si_3N_4. In this paper, we report our observations on *h*-BN–SiC interphase boundaries in these composites and discuss them in the light of models for the formation of intergranular amorphous films in ceramic materials, geometric considerations for low interfacial energies and the possible bonding at *h*-BN–SiC interfaces free of intergranular films. Finally, we will draw a comparison between the observations reported here of *h*-BN–SiC interfaces and observations of *h*-BN–β-Si_3N_4 interfaces that we have reported elsewhere.[13]

2. Experimental procedure

Si_3N_4–SiC composites were prepared by first mixing commercially available SiC and Si_3N_4 powders without the addition of any sintering aids and then subjecting powder compacts to hot isostatic pressing in tantalum cans at 2373 K for 1 h under 200 MPa argon pressure to achieve composite densification.[14,15] Two of the green compacts were deoxidised in a graphite furnace at 2173 K prior to hot isostatic pressing to eliminate the surface

* Corresponding author. Tel.: +44-1223-334-312; fax: +44-1223-334-567.
E-mail address: kmk10@cam.ac.uk (K.M. Knowles).

0955-2219/02/$ - see front matter
PII: S0955-2219(01)00481-2

silica. The sub-micron size *h*-BN grains arose indirectly during the densification process from boron oxide present on the surface of fine particles of boron nitride sprayed onto the internal surface of the tantalum can to prevent an unwanted chemical reaction between SiC and the tantalum.[14]

Slices from the hot isostatically pressed composites were thinned mechanically and ion milled for transmission electron microscopy (TEM). The specimens were examined in a Jeol 2000FX at 200 kV and in a Jeol 4000EX-II at 400 kV which has a spherical aberration coefficient, C_s, of 1 mm and a point-to-point resolution of ≈1.7 Å.

3. Experimental results and interpretation

3.1. h-*BN–SiC interphase boundaries in composites made from as-received powders*

The most frequent observation of *h*-BN–SiC interphase boundaries in these composites revealed by electron diffraction and high resolution transmission electron microscopy was that both within SiC grains and at SiC grain boundaries, {0001} planes in the *h*-BN precipitates aligned themselves parallel either to {111} 3C SiC planes or {0001} α-SiC planes. Examples of *h*-BN–3C SiC interphase boundaries with the beam direction parallel to [110] 3C SiC are shown in the dark field TEM image in Fig. 1 (a) where {0001} planes of two adjacent *h*-BN precipitates are parallel to $(1\bar{1}\bar{1})$ and $(1\bar{1}1)$ planes respectively of the surrounding 3C SiC grain within which twinning is apparent on one of the {111} planes. Confirmation of this orientation relationship can be found from the electron diffraction pattern in Fig. 1(b), taken from an area much larger than that shown in Fig. 1(a). An indexed schematic of Fig. 1(b) is shown in Fig. 1(c). One of the *h*-BN grains appears dark in Fig. 1(a) because of the imaging conditions: an objective aperture was placed on both the $(1\bar{1}1)$ SiC spot and the (0002) spot of the precipitate labelled h-BN_2, as shown in Fig. 1(b).

The high resolution transmission electron microscope (HRTEM) image shown in Fig. 2 (a) of the boxed area in Fig. 1(a) at this zone provides evidence for the presence of a very thin residual intergranular amorphous film at the *h*-BN–3C SiC interphase boundary. In this particular case, the film was ≈12±1 Å thick where the $(1\bar{1}1)$ SiC and the (0002) *h*-BN planes either side of the boundary were parallel to the boundary plane. Towards the right-hand side of this micrograph the end of the *h*-BN grain starts to curve, beginning at the twin boundary within the SiC grain. Evidence from HRTEM shows that in general the curved part of the *h*-BN–3C SiC boundary is *not* parallel to the electron beam because moiré fringes arising from the interference between (0002) *h*-BN and the (002) planes of the 3C SiC could be clearly seen on the HRTEM images. However, in the specific portion of the curved boundary seen in Fig. 2(a), it would appear from HRTEM that there is more likely to be overlap in projection between the 3C SiC and the intergranular glassy film alone, which is why moiré fringes are not seen here.

A further HRTEM micrograph of a *h*-BN–3C SiC boundary is shown in Fig. 2(b). The (0002) *h*-BN planes are parallel to the (111) 3C SiC planes of the region to the left of the twin plane marked with a star. Thus, the orientation relationship between the *h*-BN grain and the surrounding twinned SiC is the same as with the precipitate labelled h-BN_2 in Fig. 1(a). While there is clear evidence in Fig. 2(b) for an amorphous intergranular film to the right of the star, this film does not extend to the left of the star, in contrast to the evidence in Fig. 1(a) where the $(1\bar{1}1)$ SiC and the (0002) *h*-BN planes either side of the boundary are parallel. Furthermore, the film to the right of the star is not of a uniform thickness: the shape of the film seen in projection in the HRTEM image and the relative sharpness of the film-SiC crystal boundary is indicative of a section of a cylinder cut parallel to its axis. The alternative possibility that the shape is lens-shaped can be discounted from the nature of the contrast from the intergranular film—if the shape were lens-shaped, the strong channelling of electrons from crystalline portions overlapping in projection with amorphous regions would cause the crystalline portions to dominate the image, in the same way that, for example, small suitably oriented diamond particles can be distinguished from amorphous carbon background in the HRTEM.

Clarke[16] has proposed that amorphous intergranular films have an equilibrium thickness which is determined by the competition between attractive van der Waals forces and repulsive steric forces. While he notes that the equilibrium thickness is strongly dependent on the dielectric properties of the adjacent grains, he also notes that experimental observations of thin intergranular phases do not appear to be dependent on the angle of misorientation across the boundary and appear to be relatively constant from one boundary to another, within the accuracy of observations. The exception to this is that in boundaries of low energy, such as low-angle boundaries and twin boundaries, no intergranular phase is detectable.

While Clarke's theory[16–18] is able to account for the observation of the 12±1 Å thick amorphous film between BN and SiC when (0001) planes of BN are parallel to (111) planes of SiC [Fig. 2(a)] on the assumption that this boundary is not of low energy and that the Hamaker constant of 113 zJ for a silica film sandwiched between *h*-BN and 3C SiC calculated for such an interface[19] is indicative of the occurrence of a thin intergranular film in line with the calculations of

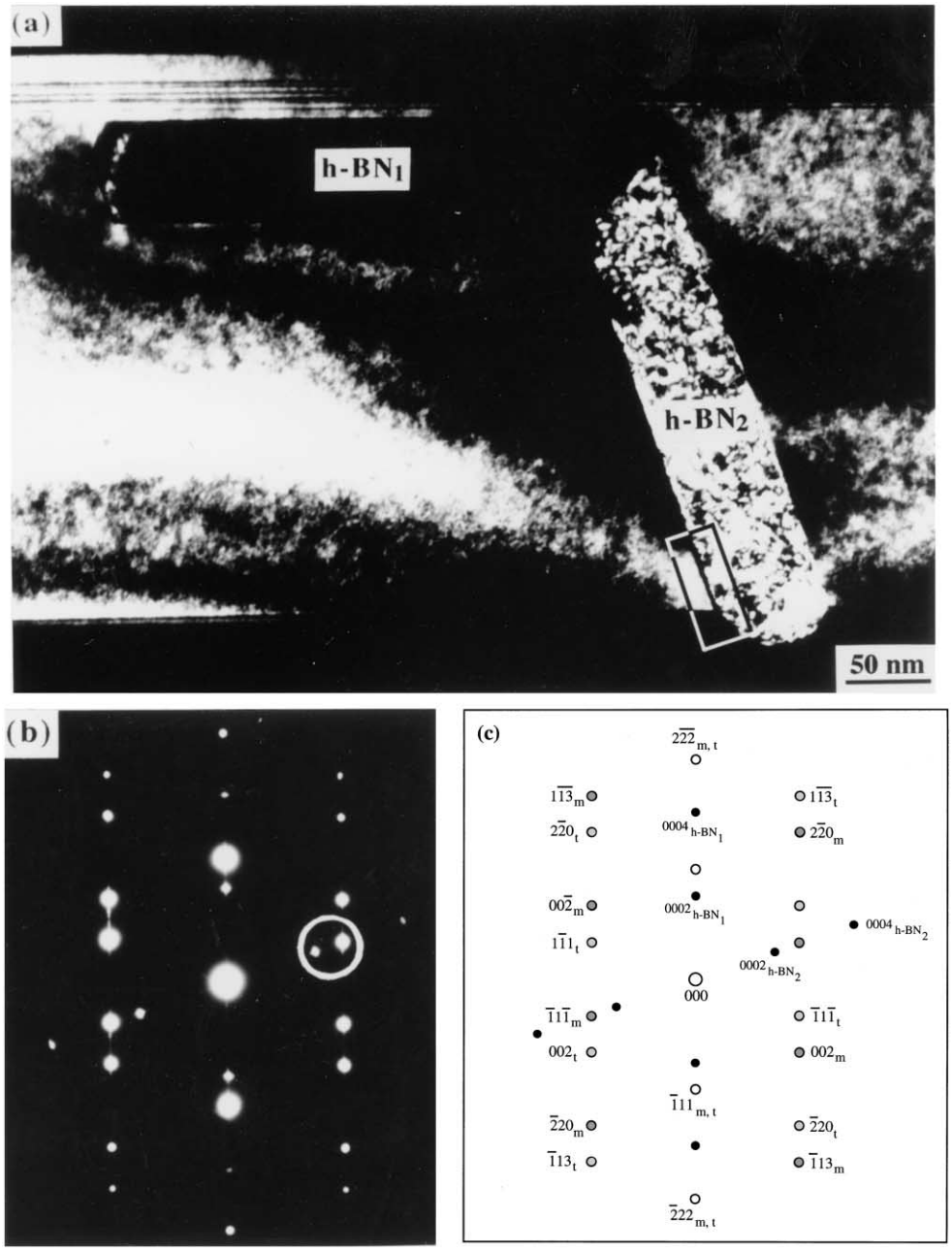

Fig. 1. (a) A dark field image of *h*-BN grains grown onto two sets of {111} 3C SiC planes. (b) A diffraction pattern obtained when the 3C SiC grain internally twinned on ($\bar{1}$11) was parallel to [110]. The position of the objective aperture used to obtain the dark field image in (a) is also shown by a white circle around two reflections in (b). (c) Indexed schematic of (b), with filled black dots denoting *h*-BN reflections, and unfilled circles other than 000 representing reflections common to the matrix (m) and twin (t) 3C SiC reflections.

Clarke,[17] it does not account for the interfacial observations in Fig. 2(b), which are in marked contrast to those in Fig. 2(a). Furthermore, while there is recent experimental evidence to show that the equilibrium film thickness is indeed dependent on the orientation of interface with respect to the highly anisotropic *h*-BN phase,[19] this does not account either for the observations in Fig. 2(b).

For the particular *h*-BN–SiC interface, a part of which is shown in Fig. 2(b), it is relevant that the length of unwetted interface is three times longer than the length of wetted interface. Furthermore, it is also relevant that the film thickness at the wetted interface has a maximum thickness of ≈38 Å. A simple calculation, in which the film at the wetted interface is distributed uniformly along the length of both the wetted and unwetted part of the interface, on the basis that the film at the wetted part has the shape of section of a cylinder cut parallel to its axis, gives a uniform equilibrium film thickness comparable within experimental uncertainties

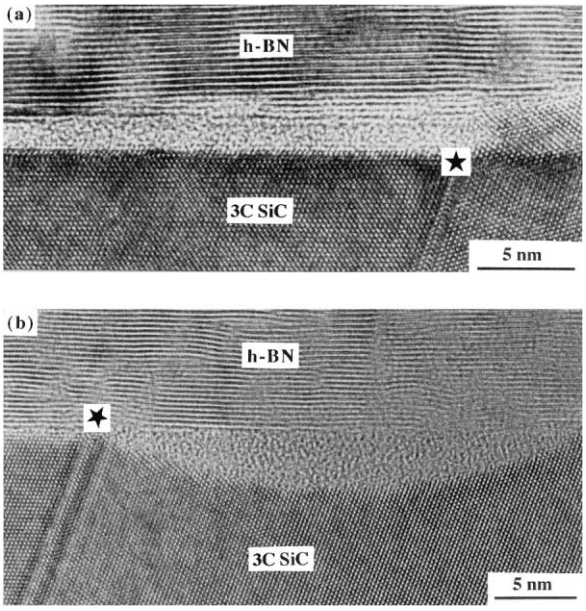

Fig. 2. HRTEM images of interphase boundaries between *h*-BN and twinned 3C SiC grains showing that wetting behaviour can be altered when a twin boundary intersects the interphase boundary. Note that the wetting behaviour in (a) is different from that shown in (b), although the orientation relationships at the points marked with * are the same. The image in (a) was obtained from the boxed area shown in Fig. 1(a).

to the 12 ± 1 Å thickness observed in Fig. 2(a). Thus, one possible explanation for the observation in Fig. 2(b) is that de-wetting has occurred at the unwetted interface, encouraged by the existence of a suitably shaped void adjacent to the wetted part where liquid squeezed out from the unwetted part could simply collect.

In the example shown in Fig. 3 (a), a *h*-BN grain is sandwiched between a 3C SiC grain and a 6H SiC grain. In this particular example, clear electron diffraction evidence [Fig. 3(b)] could be obtained to confirm that the orientation relationships between *h*-BN and SiC were:

$$\begin{aligned}&[110]_{3C\,SiC}||[11\bar{2}0]_{h\text{-}BN}\ \text{and}\ (1\bar{1}\bar{1})_{3C\,SiC}||(0001)_{h\text{-}BN}\\&[11\bar{2}0]_{6H\,SiC}||[11\bar{2}0]_{h\text{-}BN}\ \text{and}\ (0001)_{6H\,SiC}||(0001)_{h\text{-}BN}\end{aligned}\qquad(1)$$

These orientation relationships were found frequently at other BN–SiC interfaces and were by far the dominant orientation relationships observed. It is evident from Fig. 3(a) that the *h*-BN–3C SiC boundary is step-like in nature, whereas the *h*-BN–6H SiC is flat. HRTEM images from both interphase boundaries showed the presence of 12 ± 1 Å thick amorphous intergranular films,[20] consistent with the contrast in Fig. 3(a) at the interphase boundaries which is indicative of the existence of intergranular films.

The streaking evident in Fig. 3(b) arises from one dimensional disorder in both *h*-BN and the adjacent SiC parallel to the [0001] *h*-BN direction. In the (0001) 6H SiC and (111) 3C SiC systematic row of reflections, there are double arrowed strong spots corresponding to $\approx$5 Å *d*-spacings. Further double arrowed strong spots perpendicular to these between the twin spots are at $\approx$2.66 Å *d*-spacings. These double arrowed spots can be identified as (0001) and $(1\bar{1}03)$ 2H SiC reflections respectively in the $[11\bar{2}0]$ 2H SiC zone, arising from the faulting within the 3C SiC grain. Weak reflections at the single arrowed positions in Fig. 3(b) are $\{1\bar{1}01\}$ and $\{1\bar{1}03\}$ *h*-BN reflections, the structure factors of which are non-zero, and the magnitudes of which depend on the difference between the atomic scattering factors of boron and nitrogen, rather than the sum.

In contrast to the dominant orientation relationship observed represented by Eq. (1), *h*-BN–3C SiC interfaces were found where {0001} *h*-BN planes were not parallel to {111} 3C SiC planes. An example is shown in Fig. 4. This is an HRTEM image of a *h*-BN–3C SiC interface at relatively low magnification taken with the beam direction parallel to [110] 3C SiC and $[11\bar{2}0]$ *h*-BN. However, it is apparent from the electron diffraction pattern shown in Fig. 4(c) that the (0001) *h*-BN planes make angles of $\approx$16 and 55° respectively with the $(\bar{1}11)$ and $(\bar{1}1\bar{1})$ 3C SiC planes. It is also relevant that, while the 'macroscopic' interface plane in Fig. 4 between the *h*-BN and the 3C SiC is parallel to (0001) *h*-BN, microscopically it facets on the SiC side with the major 15–20 nm length facets parallel to $(\bar{1}11)$ 3C SiC and the minor 4–6 nm facets having $(\bar{1}1\bar{1})$ 3C SiC planes prominent. It is apparent in Fig. 4(c) that $(1\bar{1}02)$ *h*-BN planes are approximately parallel to $(\bar{1}1\bar{1})$ 3C SiC planes, so that this orientation relationship can be described as close to:

$$[110]_{3C\,SiC}||[11\bar{2}0]_{h\text{-}BN}\ \text{and}\ (\bar{1}1\bar{1})_{3C\,SiC}||(1\bar{1}02)_{h\text{-}BN}\qquad(2)$$

Further examination of Fig. 4(a) shows that the interphase boundary between the *h*-BN grain and the 3C SiC consists of a number of different layers. A thin *h*-BN layer can be seen adjacent to the faceted SiC and a small amount of what is most likely to be a silica-based amorphous phase[14] is trapped between the SiC and the *h*-BN. Adjacent to this $\approx$7 nm thick layer of *h*-BN on the *h*-BN side of the *h*-BN–3C SiC interface is a layer $\approx$20 nm thick with a one-dimensional disordered structure. This disordered structure, together with parallel electron energy loss spectroscopy (PEELS) of these layers showed that was turbostratic carbon.[14,21] Beyond this turbostratic carbon layer is the main *h*-BN inclusion, in which there were occasional layers with the same contrast as the $\approx$10 nm thick turbostratic carbon layer, e.g. Fig. 4(b).

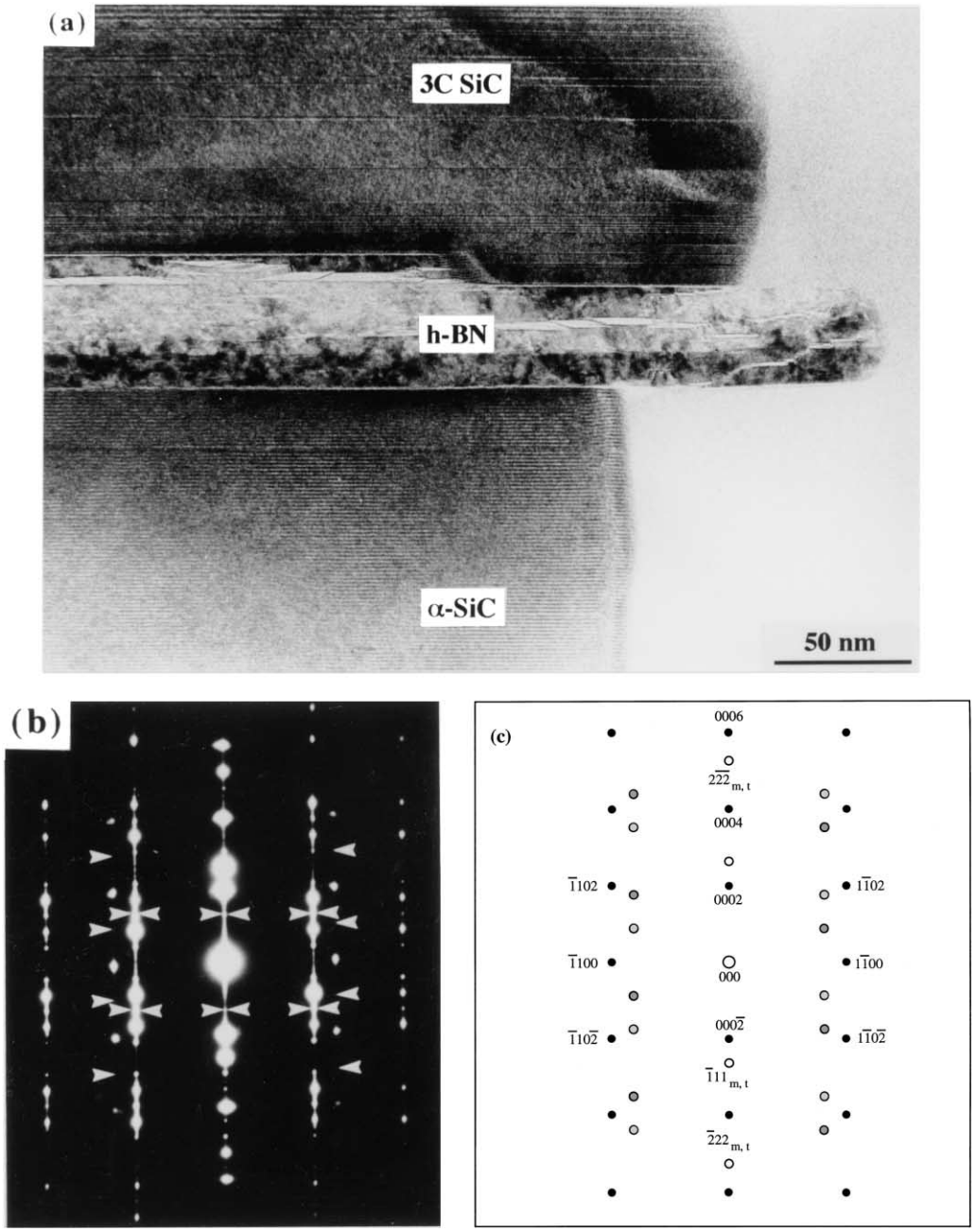

Fig. 3. (a) A bright field image of an *h*-BN grain sandwiched between a twinned 3C SiC grain and a α-SiC grain. (b) The diffraction pattern obtained when both SiC grains and the BN grain were inside the selected area aperture, showing that in the *h*-BN grain and α-SiC grain the beam direction is parallel to $[11\bar{2}0]$ and that in 3C SiC the beam direction is parallel to [110]. Double arrowed spots are (0001) and $(1\bar{1}03)$ 2H SiC reflections respectively in the $[11\bar{2}0]$ 2H SiC zone. Weak $\{1\bar{1}01\}$ and $\{1\bar{1}03\}$ *h*-BN reflections arise at the single arrowed positions. (c) Indexed schematic of (b), with four-index Miller-Bravais indices being used for the *h*-BN reflections, shown as filled black dots, and three indices used for the matrix (m) and twin (t) 3C SiC reflections.

An explanation for the occurrence of these turbostratic carbon layers co-existing with the *h*-BN consistent with the formation of the *h*-BN grains is given elsewhere.[14] Thin layers sandwiched between *h*-BN layers and also bounded by (0001) *h*-BN planes have also been observed in B_4C-BN composites by Ruh, Kearns, Zangvil and Xu[22] (e.g. Figs. 10 and 16 of their paper) who commented on the possible existence of a B(N,C) solid solution on the basis of the observation of carbon in EDS analyses of the *h*-BN regions, but did not consider the alternative possibility of amorphous or turbostratic carbon regions coexisting with the *h*-BN.

A further example where (0001) planes of *h*-BN are not parallel to (111) 3C SiC planes is shown in Fig. 5. Here the *h*-BN inclusion was entirely surrounded by the 3C SiC grain and the interface was imaged with the

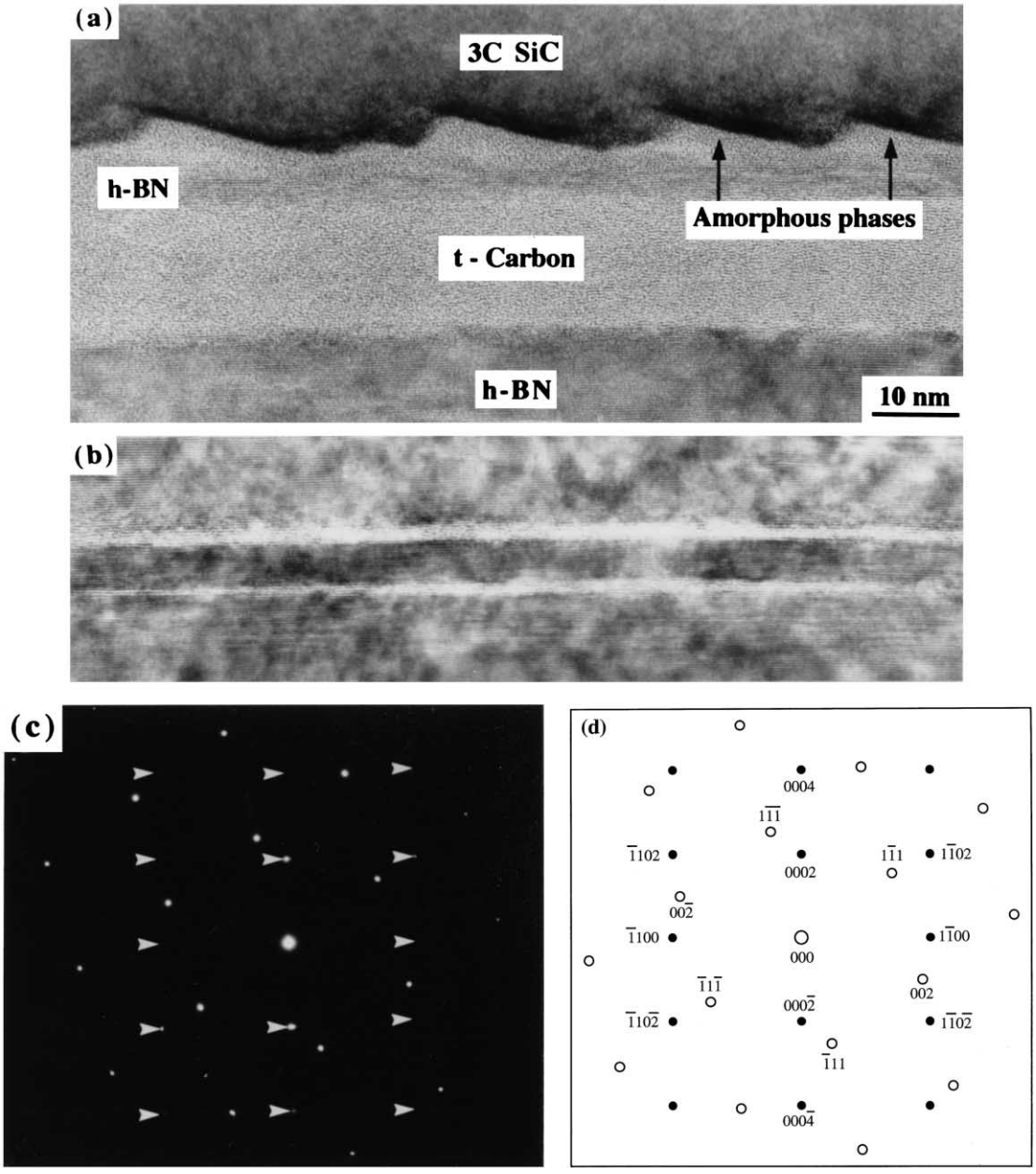

Fig. 4. (a) HRTEM image of a *h*-BN-3C SiC interphase boundary when {0001} *h*-BN planes are not parallel to a set of {111} 3C SiC planes. The main *h*-BN grain in the bottom part of this micrograph is separated from the 3C SiC grain by a thin 7 nm thick *h*-BN layer and a ≈20 nm thick turbostratic carbon layer. (b) Detail of a thin layer with a turbostratic structure within the *h*-BN grain away from the region shown in (a). (c) Diffraction pattern obtained when the 3C SiC grain and the *h*-BN grain were parallel to [110] and [1$\bar{1}$20] directions, respectively. (d) Indexed schematic of (c), with four-index Miller-Bravais indices being used for the *h*-BN reflections, shown as filled black dots, and three indices used for the 3C SiC reflections, shown as unfilled circles.

electron beam direction parallel to $[001]_{3C\,SiC}$ and $[10\bar{1}0]_{h\text{-BN}}$. It is ambiguous from the HRTEM image whether or not there is a distinct intergranular film at the *h*-BN–3C SiC interface in Fig. 5(a): viewed along a direction parallel to the interface, it is apparent that fringes from the 3C SiC extend some way into the 'amorphous' region. Furthermore, any film thickness inferred from this image is less than the ≈12 Å film thickness seen at the majority of *h*-BN–3C SiC interfaces.

It is apparent from Fig. 5(a) and (b) that $\{100\}_{3C\ SiC}$ planes are parallel to the $\{0001\}_{h\text{-BN}}$ basal planes. A schematic of the diffraction pattern obtained from the interphase boundary region is shown in Fig. 5(c), from which it can be seen that this orientation relationship is one which is different from the one for the interface shown in Fig. 4 and which maximises the point group symmetry of the intersection point group of the interphase boundary: the intersection point group is *mmm*, the point group symmetry of *h*-BN is 6/*mmm* and the

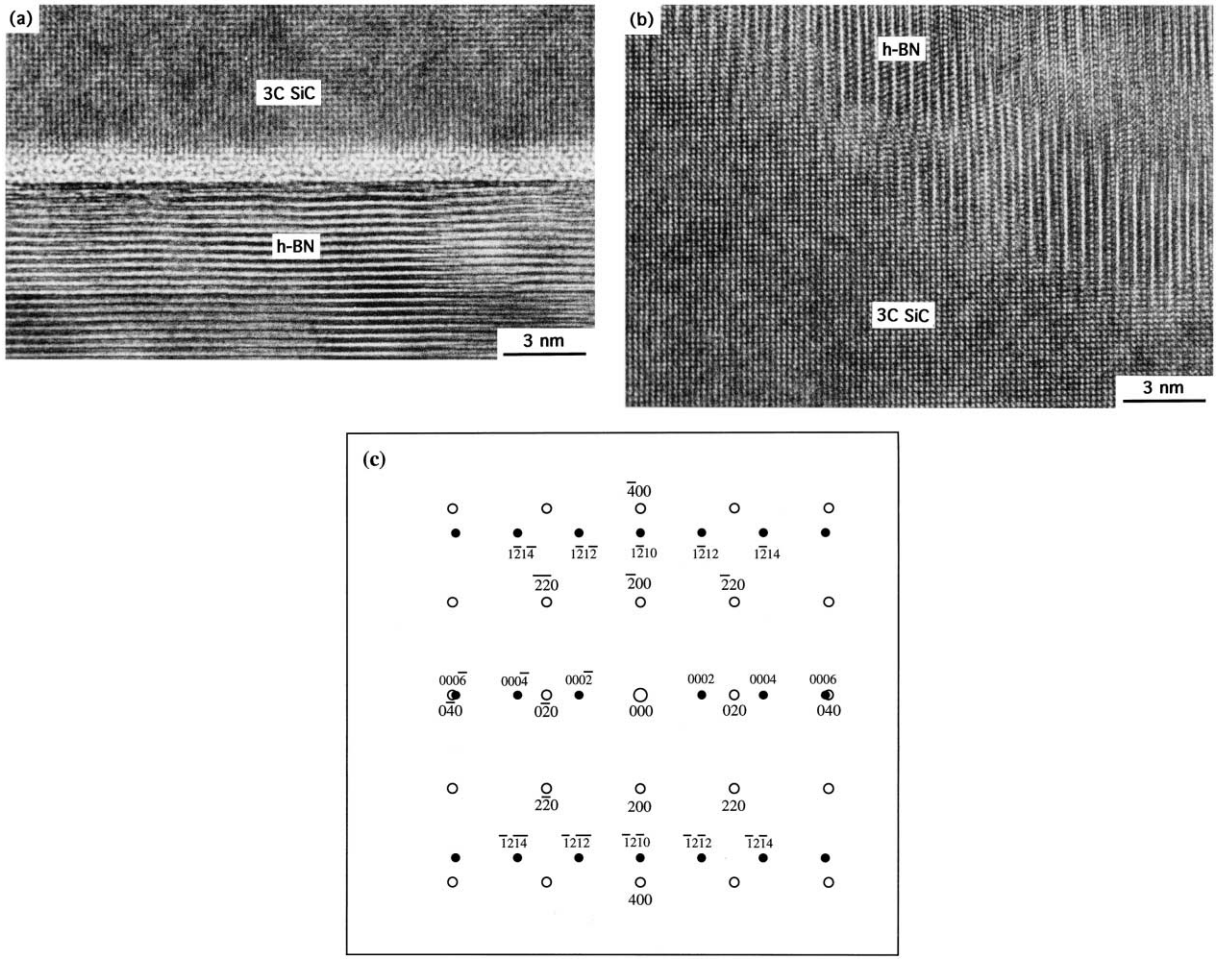

Fig. 5. HRTEM images of *h*-BN–3C SiC interphase boundaries from an *h*-BN inclusion entirely surrounded by a 3C SiC grain. In (a), the *h*-BN–3C SiC interface is parallel to $(0001)_{h\text{-BN}}$, whereas in (b) there is overlap in projection of the *h*-BN and 3C SiC grains at the interface. (c) An indexed schematic of the electron diffraction pattern from this region, showing that the electron beam direction is parallel to $[001]_{3C\ SiC}$ and $[10\bar{1}0]_{h\text{-BN}}$, with $(020)_{3C\ SiC}$ parallel to $(0002)_{h\text{-BN}}$. Four-index Miller-Bravais indices are used for the *h*-BN reflections, shown as filled black dots, and three indices used for the 3C SiC reflections, shown as unfilled circles.

point group symmetry of 3C SiC is $\bar{4}3m$. This 'special' orientation relationship may help to account for the lack of clear evidence of an amorphous intergranular film in Fig. 5(a).

3.2. Interphase boundaries in composites made from deoxidised powders

In comparison to the *h*-BN inclusions seen in the composites made from as-received powders, the inclusions in the relatively porous composites made from deoxidised powders had fewer dislocations and cracks and the (0002) *h*-BN planes were markedly less buckled. These inclusions were only found at interfaces between grains, rather than both within and between grains, as in the composites made from as-received powders. Examples of *h*-BN–SiC interfaces in these latter composites are shown in Figs. 6 and 7. PEELS analyses, such as the one shown in Fig. 6, confirmed that these inclusions were *h*-BN, rather than the remnants of carbon resin used as a deoxidant crystallising as graphite. The relative perfection of the *h*-BN inclusions was consistent with the high levels of porosity in these composites, helping to relieve thermal strains in the *h*-BN lattice arising during cooling after the hot isostatic pressing heating schedule.[23] It is also possible that the absence of oxygen in the deoxidised compact is beneficial for the formation of defect free *h*-BN layers: in carbon, the ability for graphitization to occur increases with decreasing oxygen content,[24] and it is possible that a similar phenomenon occurs for *h*-BN, given the similarity in chemistry of these two phases.

It is to be noted that the *h*-BN grain in Fig. 6 is sandwiched between two α-SiC grains, although there is a thin slab of 3C SiC on one side of the *h*-BN grain. Unlike in the composites made from as-received powders, the α-SiC in these composites remained largely untransformed after hot isostatic pressing.[25] In Fig. 6, the electron beam direction is parallel to $[11\bar{2}0]_{\alpha\text{-SiC}}$, and while it is evident that the basal α-SiC planes are parallel to the basal *h*-BN planes, the

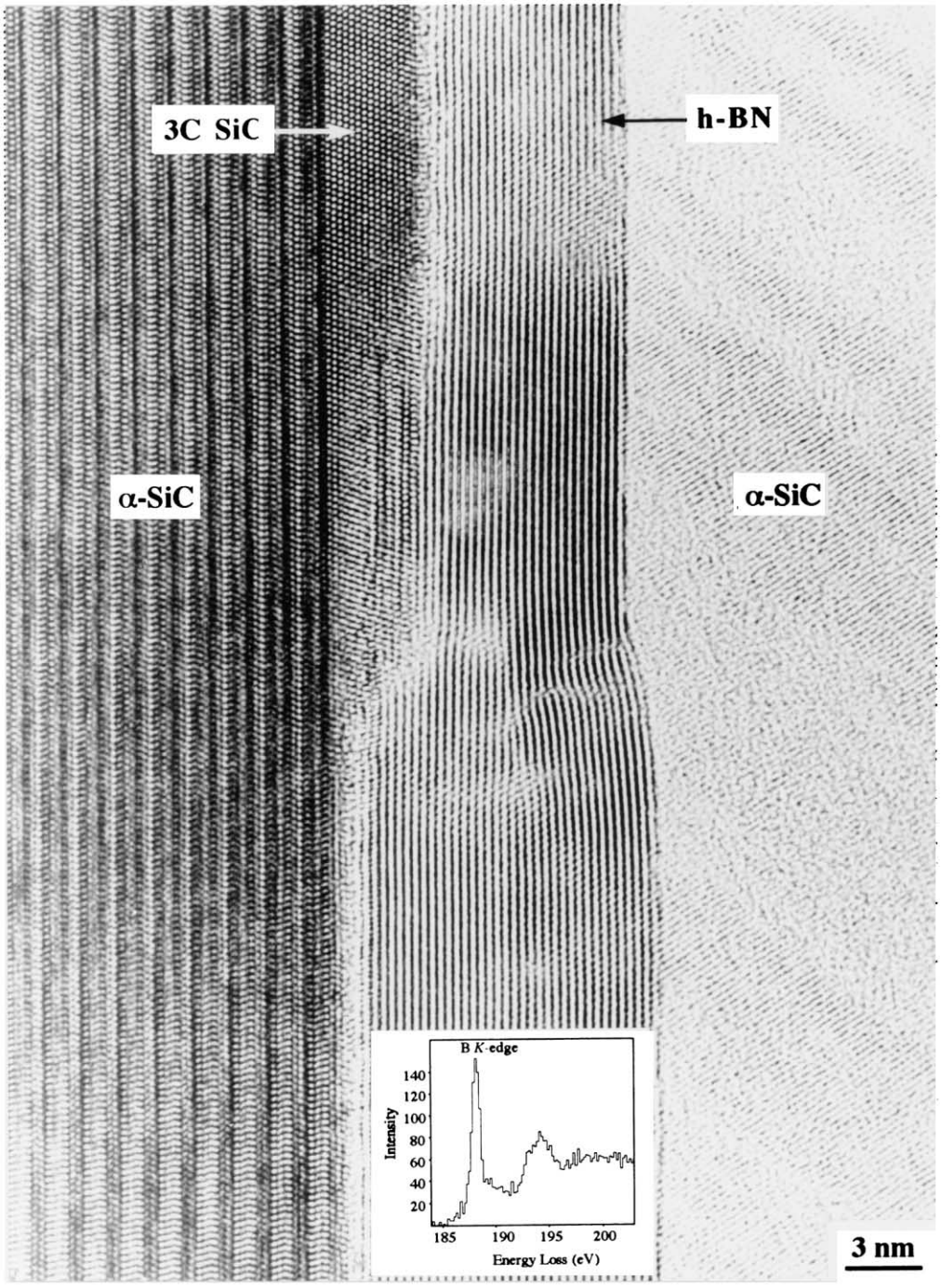

Fig. 6. An HRTEM image of a *h*-BN grain sandwiched between two α-SiC grains in the SiC–Si_3N_4 composites made from deoxidised compacts. The PEELS spectrum in the inset shows the B *K*-edge obtained from the *h*-BN grain. Note the apparent lack of an amorphous intergranular film between *h*-BN and SiC.

electron beam is not parallel to any low index *h*-BN direction. The *h*-BN–SiC interphase boundary appears to be free of an intergranular film, but is not planar. Two other examples of typical interphase boundaries observed between *h*-BN and SiC grains in the composites made from deoxidised powders are shown in Fig. 7. These also show a lack of intergranular film, with a clear preference for (0001) *h*-BN planes to be parallel to (0001) α-SiC planes.

In principle, deoxidation of the silicon carbide and silicon nitride powders prior to sintering should be beneficial, in that intergranular film formation is prevented. Hence, if they can be made fully dense, the resultant composites should exhibit superior creep properties at high temperature in comparison with, composites with remnant intergranular phase. However, it was found that densification was severely impeded in the composites

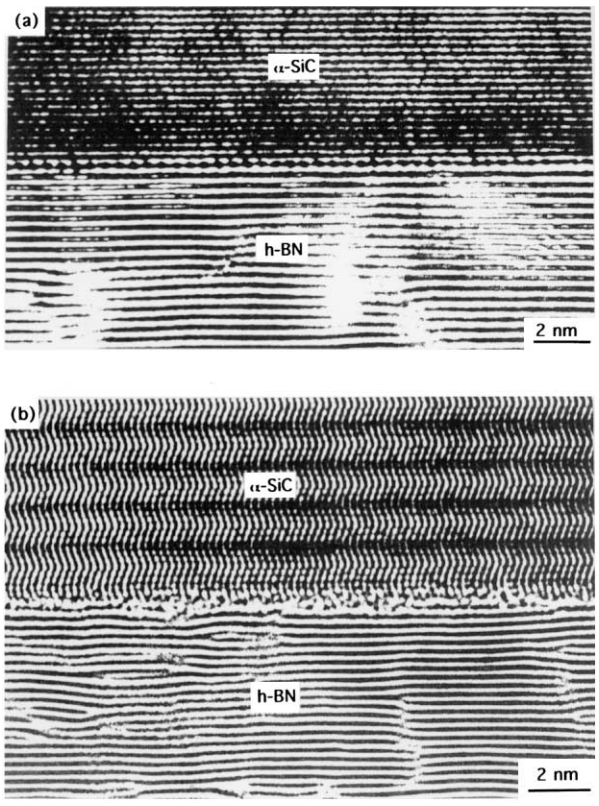

Fig. 7. (a) and (b) Two further examples of interphase boundaries between *h*-BN and α-SiC grains in the SiC–Si_3N_4 composites made from de-oxidised compacts. These also show a lack of an amorphous intergranular film and a clear preference for (0001) *h*-BN planes to be parallel to (0001) α-SiC planes.

made with the deoxidised powders, producing composites which were much more porous than the ones made with as-received powders.[12,15] This was because of the relative lack of liquid phase sintering which produced a porous, fine grained, microstructure in these composites.[15] Thus, the advantages to be gained in principle in using deoxidised powders in terms of possible improved high temperature creep resistance for a dense material are outweighed heavily by the lack of densification, producing material with poorer flexural strength as a consequence. The lack of densification and lack of grain growth evident in the composites made from de-oxidised powders is consistent with the observation that the *h*-BN inclusions were not observed inside either SiC or Si_3N_4 grains in these composites. By comparison, the extensive grain growth of the 3C SiC in the composites made from the as-received powders was able to engulf both *h*-BN inclusions and small Si_3N_4 precipitates within 3C SiC grains.[12,15]

4. Discussion

The general tendency that can be deduced from our experimental observations is that *h*-BN–SiC interfaces show evidence for thin amorphous intergranular films in the SiC–Si_3N_4 composites made from as-received powders, but not those made from deoxidised powders. We have argued elsewhere that this is related quite straightforwardly to the volume of liquid phases present during consolidation at high temperature in the two types of composite.[12] Thus, the impression gained from our observations is that if silicaceous liquid phases are present at high temperature, a remnant intergranular amorphous film of a characteristic thickness can, and will, be adopted on cooling to room temperature.

The further observation that there is a alignment of (111) 3C SiC and (0001) α-SiC planes with (0001) *h*-BN planes both with and without intergranular amorphous films also merits comment. A simple qualitative explanation is that since a number of SiC grains in the composites are bounded either by {111} 3C SiC or (0001) α-SiC planes, the chemical reactions forming the *h*-BN particles do so in a manner whereby basal plane 'meshes' of *h*-BN are deposited on available low energy SiC planes, leading to inclusions where growth normal to [0001] is relatively difficult, but where the meshes can grow relatively rapidly within the (0001) planes. Similar qualitative explanations are effective in accounting for other preferred orientations, such as those seen in thin films of cubic close packed metals vapour deposited on flat substrates of amorphous silica[26] and zinc oxide films sprayed onto both crystalline and amorphous substrates.[27–30]

In striving to provide a more quantitative explanation, it is instructive to examine crystallographic and atomic bonding aspects of *h*-BN–SiC interfaces free of amorphous phases, to see if there is any rationale for the selection of 'low energy' orientation relationships. While caution must be exercised in the use of geometric criteria for low interfacial energies (see, for example, Sutton and Balluffi[31]), it is nevertheless useful to determine crystallographic features of heterophase interfaces in terms of the near-coincidence concept[32] to try and determine what orientation relationships might arise. In this approach, the details of atomic bonding at the interfaces are necessarily of secondary importance, although ultimately the adoption of any particular three-dimensional orientation relationship will be determined by the way in which atoms bond at the interfaces. Nevertheless, as Champion and Hagège have recently demonstrated in their analysis of ZrB–ZrB_2 interfaces,[33] the application of the coincidence approach can prove to be very useful in understanding complex interfacial structures.

We have, therefore, used the Bonnet and Cousineau computation method[34] for near-coincident cell generation to search for near-coincidence cells in *h*-BN and 3C SiC. For these calculations, we have taken the lattice parameters of *h*-BN to be $a = 2.5044$ Å, $c = 6.6562$ Å and the lattice parameter of 3C SiC to be 4.358 Å. We have further chosen lattice 1 to be 3C SiC and lattice 2

to be *h*-BN. Possible near-coincident cells *M*1 and *M*2 for lattices 1 and 2 respectively and other related crystallographic quantities are given in Table 1. These 20 crystallographically distinct relationships were determined using the calculation parameters $\Sigma_{1\ \max}=17$, $\Delta L=0.9$ Å, $S_{\max}=0.4$, $\Delta u=0.3$ and $\Delta\theta=0.003$ rad using the notation of Bonnet and Cousineau. Here, Σ_1 is the ratio of the volume of the near-coincident cell of 3C SiC to the volume of the conventional cubic *F* unit cell of 3C SiC, ΔL is the maximum allowed mismatch in length between two corresponding vectors $\mathbf{V}^1$ and $\mathbf{V}^2$ in lattices 1 and 2 which can be chosen to be parallel for computational purposes, $S_{\max}$ is the maximum allowed sum of the magnitudes of the principal strains involved in relating formally the near-coincident cells of the two lattices, Δu has to take a value less than 0.5 and is related to the formalism describing mathematically the slight mismatch of corresponding near-coincident cells, and $\Delta\theta$ is a suitably small angular increment used in the computation method to generate rotations about suitable $\mathbf{V}^1 \parallel \mathbf{V}^2$.

For each relationship in Table 1, the matrix $[U]_{\mathrm{F1}}$ relates components of vectors $\mathbf{v}_2$ referred to lattice 2 to components of vectors $\mathbf{v}_1$ referred to lattice 1 through the formula

$$\mathbf{v}_1 = [U]_{\mathrm{F1}}\ \mathbf{v}_2 \tag{3}$$

and similarly three-index plane normal descriptions, $\tilde{\mathbf{n}}$, represented as row vectors, are related through the formula

$$\tilde{\mathbf{n}}_2 = \tilde{\mathbf{n}}_1[U]_{\mathrm{F1}} \tag{4}$$

Thus, for NCSL Pair No. 1, where $\Sigma_1=3$ and $\Sigma_2=8$, and where *S*, the sum of the magnitudes of the principal strains ε_1, ε_2 and $\varepsilon_3=0.153$, less than $S_{\max}$, the column vectors of the near-coincident cell *M*2 are related to the column vectors of the near-coincident cell *M*1 through Eq. (3). Furthermore, using Eq. (4), $(040)_1$ is related to $(00\bar{6})_2$ and $(400)_1$ is related to $(1\bar{2}0)_2$ for this particular near-coincident site relationship. Consideration of the variants on this relationship arising from the symmetries of the respective structures shows that this near-coincident site lattice description is one which can be used for the orientation relationship shown in Fig. 5. An alternative near-coincident site lattice description, and one which would produce smaller strains for the orientation relationship shown in Fig. 5, is given by NCSL Pair No. 9 in Table 1. Here, $S=0.067$, and $(040)_1$ is again related to $(00\bar{6})_2$, but $(10,\ 0,\ 0)_1$ is related to $(3\bar{6}0)_2$, rather than $(2.5, \bar{5}, 0)_2$ as it would be through NCSL Pair No. 1.

While either NCSL Pair No. 1 or No. 9 could conceivably provide a geometrical justification for the occurrence of the orientation relationship shown in Fig. 5 between SiC and *h*-BN, attempts to rationalise the dominant experimental orientation relationship of $[110]_{3\mathrm{C\ SiC}} \parallel [11\bar{2}0]_{h\text{-BN}}$ with $(1\bar{1}\bar{1})_{3\mathrm{C\ SiC}} \parallel (0001)_{h\text{-BN}}$ (i.e. $[110]_{3\mathrm{C\ SiC}} \parallel [110]_{h\text{-BN}}$ with $(1\bar{1}\bar{1})_{3\mathrm{C\ SiC}} \parallel (001)_{h\text{-BN}}$ in three index hexagonal indices) using this approach were markedly less successful. None of the near-coincident relationships in Table 1 can account for this.

In order to confirm this apparent lack of a suitable NCSL description, the computer program used to generate the NCSLs was adapted to examine in detail particular orientation relationships, rather than attempting to sample all possible orientations between *h*-BN and 3C SiC. Thus, either (i), $[001]_{h\text{-BN}}$ was matched to $[111]_{3\mathrm{C\ SiC}}$ to provide the parallel vectors $\mathbf{V}^1$ and $\mathbf{V}^2$ around which rotations could be made to search for NCSLs, or (ii), $[500]_{h\text{-BN}}$ was matched to $[022]_{3\mathrm{C\ SiC}}$ for the same purpose. This latter modification could also be used to ascertain whether the experimental orientation relationship shown in Fig. 4 had any suitable NCSL description.

In the former modification, $[001]_{h\text{-BN}}$ has a magnitude of 6.66 Å while $[111]_{3\mathrm{C\ SiC}}$ has a magnitude of 7.55 Å. Confining a search to $\Sigma_{1\ \max}=17$, $S_{\max}=0.21$, $\Delta u=0.3$ and $\Delta\theta=0.003$ rad did not produce a suitable NCSL description at all. Widening the search by letting $\Sigma_{1\ \max}=30$ produced the single NCSL description shown as NCSL Pair No. 21 in Table 2. However, this cannot account for the dominant experimentally observed orientation relationship because $[700]_2$ is related to $[21\bar{3}]_1$, $[770]_2$ is related to $[\bar{1}3\bar{2}]_1$ and $[070]_2$ is related to $[\bar{3}21]_1$, rather than $\langle 100\rangle_2$ vectors being related to $\langle\bar{1}10\rangle_1$ vectors. Thus, for NCSL Pair No. 21 there is a rotation about 19.1° relative to the dominant experimentally observed orientation relationship.

In the latter modification, $[500]_{h\text{-BN}}$ has a magnitude of 12.52 Å while $[022]_{3\mathrm{C\ SiC}}$ has a magnitude of 12.33 Å, so that the misfit between these two vectors is relatively small. However, searching using $\Sigma_{1\ \max}=17$, $S_{\max}=0.21$, $\Delta u=0.3$ and $\Delta\theta=0.003$ rad failed to produce a suitable NCSL description, as did $\Sigma_{1\max}=30$, $S_{\max}=0.21$, $\Delta u=0.25$ and $\Delta\theta=0.003$ rad.

Hence, we conclude from the NCSL analysis that the qualitative explanation whereby the {111} 3C SiC planes effectively act as templates on which the *h*-BN basal plane meshes deposit and grow is probably a reasonably good description of the actual process both in composites made from as-received powders and composites made from deoxidised powders. Accounting for the dominant experimental orientation relationship in formal geometric terms on the assumption that there is no liquid phase present at the interface necessarily requires large misfits within the parallel $(1\bar{1}\bar{1})_{3\mathrm{C\ SiC}}$ and $(0001)_{h\text{-BN}}$ planes, which is why the NCSL approach produces a null result for the experimental orientation relationship within the constraints we have specified

Table 1
Near-coincident cells for 3C SiC (lattice 1) and *h*-BN (lattice 2)[a]

NCSL Pair No.	Σ_1	Σ_2	$M1$[b]			$M2$[b]			$\varepsilon_1, \varepsilon_2, \varepsilon_3$[c]	N	$[U]_{F1}$ ($\times N$)[d]		
1	3	8	1	−1	0	4	−2	0	−0.130	4	1	−2	0
			0	0	−3	0	1	0	−0.018		0	0	−6
			2	−1	0	0	0	2	0.005		2	0	0
2	3	8	1	−1	−1	4	−2	−2	−0.169	4	1	−2	−1
			0	0	−3	0	1	0	0.005		0	0	−6
			2	−1	−1	0	0	2	0.029		2	0	0
3	4	9	−1	−1	0	3	0	0	−0.074	3	−1	−1	0
			1	−1	1	0	3	0	−0.053		1	−1	3
			1	1	1	0	0	1	0.160		−1	1	3
4	4	9	1	−2	1	3	0	0	−0.111	3	1	−2	−1
			1	0	−1	0	3	−2	−0.053		1	0	−3
			1	0	1	0	0	1	0.209		1	0	3
5	6	16	0	0	−6	2	−1	0	−0.130	4	0	0	−6
			0	1	−1	0	2	0	−0.086		0	2	−1
			1	−1	0	0	0	4	0.079		2	−1	0
6	7	16	2	−2	−3	8	−6	−6	−0.033	8	2	−4	−6
			−1	1	−2	0	1	0	0.005		−1	2	−11
			4	−3	−3	0	0	2	0.031		4	0	0
7	7	16	2	−2	−1	4	0	−3	−0.060	4	2	−2	2
			1	1	0	0	4	0	−0.039		1	1	3
			−1	0	2	0	0	1	0.109		−1	0	5
8	7	16	0	−1	−3	2	0	0	−0.130	4	0	−1	−6
			0	2	−1	0	4	0	−0.012		0	2	−2
			1	−1	0	0	0	4	0.165		2	−1	0
9	9	20	3	−3	0	10	−8	0	−0.018	10	3	−6	0
			0	0	−3	0	1	0	0.005		0	0	−15
			5	−4	0	0	0	2	0.044		5	0	0
10	9	20	3	−3	−2	10	−8	−6	−0.031	10	3	−6	−1
			0	0	−3	0	1	0	0.055		0	0	−15
			5	−4	−3	0	0	2	0.059		5	0	0
11	12	25	2	−2	−2	5	0	−3	−0.056	5	2	−2	−4
			1	2	−1	0	5	0	0.058		1	2	−2
			2	−1	0	0	0	1	0.100		2	−1	6
12	13	25	−2	1	1	5	0	0	0.024	5	−2	1	6
			1	−3	1	0	5	−1	0.005		1	−3	2
			2	0	1	0	0	1	0.100		2	0	5
13	13	25	2	−3	0	5	0	−3	−0.040	5	2	−3	0
			1	0	−2	0	5	−2	0.052		1	0	−7
			2	1	−1	0	0	1	0.178		2	1	3
14	13	32	−3	1	3	8	0	−5	−0.066	8	−3	2	9
			1	−2	0	0	4	0	−0.032		1	−4	5
			3	0	−1	0	0	1	0.029		3	0	7
15	13	32	0	2	−1	4	0	−2	−0.130	4	0	2	−2
			−1	1	3	0	4	0	−0.004		−1	1	5
			2	−1	0	0	0	2	0.076		2	−1	2
16	13	32	0	−2	3	2	0	0	−0.177	4	0	−2	3
			1	−1	−1	0	4	0	−0.002		2	−1	−1
			0	1	5	0	0	4	0.133		0	1	5
17	13	32	0	−1	−5	2	0	0	−0.130	4	0	−1	−5
			0	2	−3	0	4	0	−0.055		0	2	−3
			1	−1	0	0	0	4	0.131		2	−1	0

(*continued on next page*)

Table 1 (*continued*)

NCSL Pair No.	Σ_1	Σ_2	$M1$[b]			$M2$[b]			$\varepsilon_1, \varepsilon_2, \varepsilon_3$[c]	N	$[U]_{F1}$ $(\times N)$[d]		
18	14	27	0	−1	4	3	0	0	−0.085	3	0	−1	4
			0	−1	−3	0	3	0	0.119		0	−1	−3
			2	−1	0	0	0	3	0.160		2	−1	0
19	15	32	1	−2	2	4	0	−2	−0.082	4	1	−2	3
			2	−1	−2	0	4	−2	−0.066		2	−1	−3
			1	1	1	0	0	2	0.098		1	1	4
20	16	36	3	−3	−2	6	0	−4	−0.109	6	3	−3	0
			1	2	0	0	6	0	0.031		1	2	4
			−1	−1	2	0	0	1	0.107		−1	−1	8

[a] Computations performed for $\Sigma_{1\,max} = 17$, $\Delta L = 0.9$ Å, $S_{max} = 0.4$, $\Delta u = 0.3$ and $\Delta\theta = 0.003$ rad in the NCSL notation used by Bonnet and Cousineau.[34]

[b] The columns of $M1$ and $M2$ define base vectors of possible near-coincident cells for lattices 1 and 2 respectively.

[c] ε_1, ε_2, and ε_3 are the principal strains which when applied to the near-coincident cell for lattice 2 produce the shape of the near-coincident cell for lattice 1.

[d] $[U]_{F1}$ relates the components of vectors referred to lattice 2 to components referred to lattice 1 through Eq. (3) in the text.

Table 2
Near-coincident cell for 3C SiC (lattice 1) and *h*-BN (lattice 2) formed by matching for computational purposes the vectors $[001]_{h\text{-BN}}$ and $[111]_{3C\ SiC}$[a]

NCSL Pair No.	Σ_1	Σ_2	$M1$			$M2$			$\varepsilon_1, \varepsilon_2, \varepsilon_3$	N	$[U]_{F1}$ $(\times N)$		
21	18	49	2	−1	6	7	−2	0	−0.070	7	2	−3	6
			1	0	6	0	1	0	−0.070		1	2	6
			−3	1	6	0	0	7	−0.028		−3	1	6

[a] Computations performed for $\Sigma_{1\,max} = 30$, $S_{max} = 0.21$, $\Delta u = 0.3$ and $\Delta\theta = 0.003$ rad in the NCSL notation used by Bonnet and Cousineau.[34]

above. This suggests that the preferred orientation relationship observed in this study is not one which can be expected to be of low energy. Hence, it is not unsurprising that, when there is a sufficient amount of liquid available during sintering at high temperature, such interfaces are wetted by the liquid, with the result that on cooling remnant amorphous silicaceous material is left as a thin intergranular film.

In terms of specific models of bonding between (0001) *h*-BN planes and either {111} 3C SiC or {0001} α-SiC planes, the strong sp^2-type bonding within the (0001) *h*-BN planes contrasts with the strong sp^3-type bonding in SiC. Simple symmetry considerations might suggest that in the absence of liquid phases, the low energy {111} 3C SiC and {0001} α-SiC planes would encourage (0001) *h*-BN planes to deposit with an orientation relationship given by (1). However, in terms of simple interfacial misfits this cannot be a low misfit orientation: the repeat distance of 3.08 Å for the hexagonal mesh within these SiC planes contrasts with the *a* lattice repeat of 2.5044 Å for *h*-BN. While it could be argued that two dimensional supercells of the hexagonal SiC mesh and (0001) *h*-BN match well (since 4×3.08 Å≈5×2.5044 Å, giving low misfit), in the absence of any atomistic calculations to provide further insight, it would be prudent to conclude that the orientation relationship given by (1) might be one of relatively low energy when the interface plane is parallel to (0001) *h*-BN, but that in absolute terms, it is unlikely to be a low energy interfacial configuration.

It is interesting to compare the observations reported here of *h*-BN–SiC interfaces with observations of *h*-BN–β-Si_3N_4 interfaces, details of which we have reported elsewhere.[13] These interfaces from the same set of samples used for transmission electron microscopy of *h*-BN–SiC interfaces exhibited a number of characteristic orientation relationships between *h*-BN and Si_3N_4. Significantly, HRTEM showed that in composites made from as-received powders, the *h*-BN–β-Si_3N_4 boundaries tended not to contain any intergranular film, in contrast to the observations of *h*-BN–SiC interfaces we have reported here.

The NCSL approach is markedly more successful in being able to rationalise experimentally observed *h*-BN–β-Si_3N_4 orientation relationships than for *h*-BN–SiC interfaces. Thus, for example, we reported *h*-BN–β-Si_3N_4 HRTEM observations where there were two particular orientation relationships:[12,13]

$$[1\bar{1}20]_{h\text{-BN}} \| [\bar{1}2\bar{1}3]_{\beta\text{-}Si_3N_4} \text{ and } (0001)_{h\text{-BN}} \| (10\bar{1}0)_{\beta\text{-}Si_3N_4} \quad (5)$$

and

Table 3
Two particular near-coincident cells for *h*-BN (lattice 1) and β-Si_3N_4 (lattice 2)[a]

NCSL Pair	Σ_1	Σ_2	$M1$			$M2$			$\varepsilon_1, \varepsilon_2, \varepsilon_3$	N	$[U]_{F1}$ ($\times N$)		
A	12	3	4	−2	0	3	−1	−1	−0.080	3	4	−2	4
			−6	3	3	0	1	0	0.011		−6	3	3
			0	−1	0	0	0	1	0.069		0	−3	0
B	7	2	1	1	1	2	0	0	−0.156	2	1	2	2
			3	2	0	0	1	0	−0.017		3	4	0
			−2	1	0	0	0	1	0.047		−2	2	0

[a] Computations performed for $a = 2.5044$ Å and $c = 6.6562$ Å for *h*-BN and $a = 7.6044$ Å and $c = 2.9075$ Å for β-Si_3N_4.

$$[11\bar{2}0]_{h\text{-BN}} \| [0001]_{\beta\text{-}Si_3N_4} \text{ and } (0001)_{h\text{-BN}} \; 3.5^\circ - 4^\circ \text{ from } (10\bar{1}0)_{\beta\text{-}Si_3N_4} \quad (6)$$

A search for near-coincident cells between *h*-BN and β-Si_3N_4 is able to find a number of orientation relationships with low misfits. Details of two particular near-coincidence geometries are given in Table 3 relevant to the orientation relationships in (5) and (6).

A consideration of NCSL Pair *A* shows that the Σ values and the misfits are encouragingly low, with only a small difference in volume of corresponding cells. From the form of the matrix $[U]_{F1}$ and using Eqs. (3) and (4), it is apparent that $(001)_1$ is related to $(0\bar{1}0)_2$ and $[\bar{1}00]_1$ is related to $[10\bar{1}]_2$. Thus, since lattice 1 is *h*-BN and lattice 2 is β-Si_3N_4, pair *A* describes an orientation relationship which is related by symmetry operations to the one given in (5). Likewise, Pair *B* describes an orientation relationship related by symmetry to that given in (6), since $[100]_1$ is related to $[001]_2$ and $(001)_1$ is related to $(100)_2$.

5. Conclusions

Interphase boundaries between *h*-BN inclusions and adjacent SiC grains in Si_3N_4–SiC composites have been characterised using TEM based techniques. A strong tendency for (0001) *h*-BN planes to be parallel to (111) 3C SiC and (0001) α-SiC planes was found, with $[11\bar{2}0]$ *h*-BN parallel either to [110] 3C SiC or $[11\bar{2}0]$ α-SiC as appropriate. Thin 12 ± 1 Å amorphous intergranular films were found at such interfaces when there was sufficient liquid available in the composites during sintering at high temperature. Attempts to rationalise the occurrence of the dominant orientation relationship in terms of low misfit between *h*-BN and SiC were unsuccessful, in marked contrast to this as an explanation for experimental observations on *h*-BN–β-Si_3N_4 interfaces in the same composites where no remnant amorphous phases are seen. It is argued that {111} 3C SiC planes effectively act as templates on which the *h*-BN basal plane meshes deposit and grow, rather than the observed orientation relationships imply the adoption of low energy interfacial configurations.

Acknowledgements

We would like to thank Dr. S.M. Winder of The Carborundum Company, Niagara Falls, USA for the provision of the samples and for useful discussions. We would also like to thank Professors C.J. Humphreys and A.H. Windle, F.R.S., for the provision of laboratory facilities during the course of this work.

References

1. Goeuriot-Launay, D., Brayet, G. and Thevenot, F., Boron nitride effect on the thermal shock resistance of an alumina-based ceramic composite. *J. Mater. Sci. Lett.*, 1986, **5**, 940–942.
2. Lutz, E. H. and Swain, M. V., Fracture toughness and thermal shock behavior of silicon nitride-boron nitride ceramics. *J. Am. Ceram. Soc.*, 1992, **75**, 67–70.
3. Zhang, G.-J. and Ohji, T., Effect of BN content on elastic modulus and bending strength of SiC-BN *in situ* composites. *J. Mater. Res.*, 2000, **15**, 1876–1880.
4. Zhang, G.-J., Beppu, Y., Ohji, T. and Kanzaki, S., Reaction mechanism and microstructure development of strain tolerant in situ SiC-BN composites. *Acta Materialia*, 2001, **49**, 77–82.
5. Zhang, G.-J. and Ohji, T., Characterization of in situ SiC-BN composites. In *7th International Symposium "Ceramic Materials and Components for Engines" Applications in Energy, Transportation and Environment Systems*, ed. J. G. Heinrich and F. Aldinger. Wiley-VCH, Weinheim, 2001, pp. 471–476.
6. Zhang, G.-J. and Ohji, T., *In situ* reaction synthesis of silicon carbide-boron nitride composites. *J. Am. Ceram. Soc.*, 2001, **84**, 1475–1479.
7. Rice, R. W., Becher, P. F., Freiman, S. W. and McDonough, W. J., Thermal structural ceramic composites. *Ceram. Eng. Sci. Proc.*, 1980, **1**, 424–443.
8. Lewis, D. and Rice, R. W., Thermal shock fatigue of monolithic ceramics and ceramic-ceramic particulate composites. *Ceram. Eng. Sci. Proc.*, 1981, **2**, 712–718.
9. Lewis, D., Ingel, R. P., McDonough, W. J. and Rice, R. W., Microstructure and thermomechanical properties in alumina- and mullite-boron nitride particulate ceramic-ceramic composites. *Ceram. Eng. Sci. Proc.*, 1981, **2**, 719–727.
10. Petrak, D. R. and Lee, J. D., *Silicon Nitride/Boron Nitride Composite with Enhanced Fracture Toughness*. US Patent 5 324 694, 28 June 1994.

11. Sun, E. Y., Nutt, S. R. and Brennan, J. J., High-temperature tensile behavior of a boron nitride–coated silicon carbide–fiber glass–ceramic composite. *J. Am. Ceram. Soc*., 1996, **79**, 1521–1529.
12. Turan, S., *Microstructural Characterisation of Silicon Nitride—Silicon Carbide Particulate Composites*. PhD thesis, University of Cambridge, UK, 1995.
13. Turan, S. and Knowles, K. M., Interphase boundaries between hexagonal boron nitride and beta silicon nitride in silicon nitride–silicon carbide particulate composites. *J. Eur. Ceram. Soc*., 1997, **17**, 1849–1854.
14. Turan, S. and Knowles, K. M., Formation of boron nitride inclusions in hot isostatically pressed silicon nitride–silicon carbide composites. *J. Am. Ceram. Soc*., 1995, **78**, 680–684.
15. Turan, S. and Knowles, K. M., A comparison of the microstructure of silicon nitride–silicon carbide composites made with and without deoxidized starting material. *J. Microscopy*, 1995, **177**, 287–304.
16. Clarke, D. R., Grain boundaries in polyphase ceramics. *J. de Physique*, 1985, **46**(Coll. 4), 51–59.
17. Clarke, D. R., On the equilibrium thickness of intergranular glass phases in ceramic materials. *J. Am. Ceram. Soc*., 1987, **70**, 15–22.
18. Clarke, D. R., Shaw, T. M., Philipse, A. P. and Horn, R. G., Possible electrical double-layer contribution to the equilibrium thickness of intergranular glass films in polycrystalline ceramics. *J. Am. Ceram. Soc*., 1993, **76**, 1201–1204.
19. Knowles, K. M. and Turan, S., The dependence of equilibrium film thickness on grain orientation at interphase boundaries in ceramic-ceramic composites. *Ultramicroscopy*, 2000, **83**, 245–259.
20. Turan, S. and Knowles, K. M., Effect of boron nitride on the phase stability and phase transformations in silicon carbide. *J. Am. Ceram. Soc*., 1996, **79**, 3325–3328.
21. Turan, S. and Knowles, K. M., Transmission electron microscopy of BN inclusions in Si_3N_4–SiC composites. *Inst. Phys. Conf. Ser*., 1993, **138**, 387–390.
22. Ruh, R., Kearns, M., Zangvil, A. and Xu, Y., Phase and property studies of SiC–BN composites. *J. Am. Ceram. Soc*., 1992, **75**, 864–872.
23. Turan, S. and Knowles, K. M., High resolution transmission electron microscopy of the planar defect structure of hexagonal boron nitride. *Phys. Stat. Sol. (a)*, 1995, **150**, 227–237.
24. Rouzaud, J. N. and Oberlin, A., Structure, microtexture, and optical properties of athracene and saccharose-based carbons. *Carbon*, 1989, **27**, 517–529.
25. Turan, S. and Knowles, K. M., $\alpha \rightarrow \beta$ reverse phase transformation in silicon carbide in silicon nitride-particulate-reinforced-silicon carbide composites. *J. Am. Ceram. Soc*., 1996, **79**, 2892–2896.
26. Sprenger, J. P., Shirokoff, J. and Erb, U., Preferred orientations of fcc metals on amorphous silica. *Scripta Metallurgica*, 1989, **23**, 1531–1536.
27. Igasaki, Y. and Saito, H., The effects of deposition rate on the structural and electrical properties of ZnO:Al films deposited on $(11\bar{2}0)$ oriented sapphire substrates. *J. Appl. Phys*., 1991, **70**, 3613–3619.
28. Goyal, D. J., Agashe, C. M., Marathe, B. R., Takwale, M. G. and Bhide, V. G., Effect of precursor solution concentration on the structural properties of sprayed ZnO films. *J. Mater. Sci. Lett*., 1992, **11**, 708–710.
29. Kim, K. H., Park, K. C. and Ma, D. Y., Structural, electrical and optical properties of aluminum doped zinc oxide films prepared by radio frequency magnetron sputtering. *J. Appl. Phys*., 1997, **81**, 7764–7772.
30. Chang, J. F., Wang, H. L. and Hon, M. H., Studying of transparent conductive ZnO : Al thin films by RF reactive magnetron sputtering. *J. Cryst. Growth*, 2000, **211**, 93–97.
31. Sutton, A. P. and Balluffi, R. W., On geometrical criteria for low interfacial energy. *Acta Metallurgica*, 1987, **35**, 2177–2201.
32. Bonnet, R. and Durand, F., Study of intercrystalline boundaries in terms of the coincidence lattice concept. *Philos. Mag*. A, 1975, **32**, 997–1006.
33. Champion, Y. and Hagège, S., HREM analysis of a cubic-hexagonal (ZrB–ZrB_2) interface using the coincidence approach. *Acta Materialia*, 1997, **45**, 2621–2631.
34. Bonnet, R. and Cousineau, E., Computation of coincident and near-coincident cells for any two lattices—related DSC-1 and DSC-2 lattices. *Acta Crystallogr*. A, 1977, **33**, 850–856.